Automated segmentation of retinal blood vessels and identification of proliferative diabetic retinopathy

Herbert F. Jelinek

School of Community Health, Charles Sturt University, Wilson Street, Albury 2640, Australia

Michael J. Cree

Department of Engineering, University of Waikato, Hillcrest Road, Hamilton 3240, New Zealand

Jorge J. G. Leandro, João V. B. Soares, and Roberto M. Cesar, Jr.

Department of Computer Science, Creative Vision Research Group, Instituto de Matemática e Estatística—University of São Paulo, Brazil

A. Luckie

Albury Eye Clinic, Swift Street, Albury 2640, Australia

Received August 15, 2006; revised November 21, 2006; accepted December 20, 2006; posted January 5, 2007 (Doc. ID 73724); published April 11, 2007

Proliferative diabetic retinopathy can lead to blindness. However, early recognition allows appropriate, timely intervention. Fluorescein-labeled retinal blood vessels of 27 digital images were automatically segmented using the Gabor wavelet transform and classified using traditional features such as area, perimeter, and an additional five morphological features based on the derivatives-of-Gaussian wavelet-derived data. Discriminant analysis indicated that traditional features do not detect early proliferative retinopathy. The best single feature for discrimination was the wavelet curvature with an area under the curve (AUC) of 0.76. Linear discriminant analysis with a selection of six features achieved an AUC of 0.90 (0.73–0.97, 95% confidence interval). The wavelet method was able to segment retinal blood vessels and classify the images according to the presence or absence of proliferative retinopathy.

OCIS codes: 100.5010, 070.5010.

1. INTRODUCTION

Diabetes and its associated complications, including diabetic retinopathy (DR), have been identified as a significant growing global public health problem.[1] Between 22% and 36% of people with diabetes have retinopathy, and of those one-third have vision-threatening retinopathy.[2] Those with retinopathy will lose vision, leading to potential blindness and loss of quality of life if not treated.[3] In proliferative retinopathy, new blood vessels are formed that emerge from the area of the optic disk and spread toward the macula or emerge from peripheral vessels.[4] Timely intervention for diabetic retinopathy lessens the possibility of blindness.[5,6]

A. Retinal Blood Vessel Segmentation

A necessary initial step in applying shape analysis to retinal blood vessels is to segment the blood vessels from the background.[7] Segmentation algorithms for retinal blood vessels are numerous and have been described in detail elsewhere. Different approaches have explored image processing techniques such as matched filters, mathematical morphology, threshold probing, supervised classification, deformable models, and tracking.[8–14] We have developed a supervised approach for vessel segmentation based on the continuous wavelet transform (CWT), which has been shown to outperform other state-of-the-art methods with respect to receiver-operating-characteristic (ROC) analysis on public retinal image databases.[15–17] This segmentation approach is applied in the present paper for the detection of proliferative retinopathy using fluorescein-labeled images of the posterior pole. There is no difference in principle between using fluorescein-labeled images versus images obtained using a color nonmydriatic camera, as the segmentation algorithm is applied to the green channel only. The CWT is a powerful and versatile tool that has been applied in many different image processing problems, from image coding to shape analysis.[18] This success is due largely to the fact that wavelets are especially suitable for detecting edges in signals such as blood vessel borders and for performing fractal and multifractal analysis.[19–21] Fluorescein angiograms generally require parameter reconfiguration for most methods in the literature. One of the advantages of our approach is that it aims at minimizing the need for reconfiguring the automated segmentation parameters for every fluorescein im-

age by applying a supervised classification procedure that depends only on manually segmented images to compose a training set for segmentation.

B. Classification of Proliferative Diabetic Retinopathy

Research into automated assessment of optic fundus images has concentrated mainly on the identification of features associated with nonproliferative diabetic retinopathy.[22–25] Interpreting changes in the branching pattern of retinal blood vessels remains a challenge in the assessment of proliferative diabetic retinopathy (PDR). As there is no *a priori* way of identifying appropriate shape features for studying pathological changes in retinal blood vessels, the task remains to search for new shape features that add new explanatory power and diagnostic accuracy. Vessel morphology has been quantified with geometrical/metric and topological parameters such as length, angles, branching order, tree asymmetry, bending energy, fractal dimension, Sholl diagrams, and area of influence.[8,26–28] Early studies concentrated on the analysis of optic fundus blood vessel patterns using hand-drawn vessel patterns to analyze morphological features. These studies demonstrated that vessel occlusion and neovascularization could be identified using a feature parameter such as fractal dimension.[28] The Gabor wavelet used here to segment the blood vessels is very efficient through its wavelet characteristics, reducing overall computation time. The resulting vessel patterns are then characterized by several feature parameters based on the wavelet-derived information.

In the present paper we explore our previously described method for the segmentation of the retinal blood vessels.[17] We then show that the wavelet approach may also be successfully used for describing structural attributes possibly associated with PDR. As PDR is defined by a change in vessel pattern by either loss or addition of vessels within the retina, a skeletonized vessel pattern is sufficient for classification.

The shape features adopted here are based on calculating wavelet gradients from skeleton images, followed by the extraction of meaningful measures, including second wavelet moment, entropy of orientation, curvature, and fractal dimension. Such wavelet shape features have already been successfully employed for the characterization of another type of branching structure, i.e., neural cells.[29] Hence, the results reported here show that the wavelet approach is suitable for both segmentation and morphological characterization of retinal blood vessels in the context of proliferative retinopathy. PDR is characterized early by the presence of ischaemic areas, where a loss of blood vessels occurs, and later by new blood vessel formation caused by several angiogenic factors. Thus the blood vessel pattern obtained using the Gabor wavelet for retinae with PDR should be distinctly different from those retinae without PDR.

2. METHODS

A. Vessel Segmentation

1. Image Acquisition

Twenty-seven images (1024×1024 pixel) were obtained using a Topcon camera linked with IMAGE 2000 software. Of these, 16 were of proliferative retinopathy, and the remaining 11 were without proliferative retinopathy but with background retinopathy and other pathology. These images were exported as TIFF images using the OBJECT-IMAGE imaging software (http://rsb.info.nih.gov/nihimage/). The vasculatures were then manually traced and automatically segmented for further analysis.

2. Wavelet Transform for Vessel Segmentation

The wavelet transform is used for two important, different purposes in the context of the present paper: vessel segmentation and morphological characterization. First, we applied the Gabor wavelet transform, which differentiates the blood vessels from the background in conjunction with a training set based on the manually traced training images. The complete process has been described elsewhere and is summarized here.[17,27]

The property of being well localized both in the time and frequency domains makes wavelets adequate for local filtering and allows detection of localized singularities, such as blood vessels.[30] The Gabor wavelet was superimposed onto each pixel of the image at various angles and scales. To detect the blood vessels, for each scale value chosen, the transform was calculated over the range of 0 to 170 deg, at 10 deg steps, and the feature space was updated with the maximum value at each pixel position. Thus, the features used to identify vessel pixels were the maximum transform responses over all angles for different scale values (to span all possible vessel widths) and also the original pixel intensity value. The wavelet parameters associated with the Gabor wavelet (scale, frequency, elongation) were empirically determined in order to reach the best matching between wavelet and vessels. Once determined, the parameter configuration did not have to be changed from image to image and represented the final feature space for vessel segmentation.[31]

A normal transformation was applied to all features to obtain dimensionless values, which allows a comparison between features and avoids mistakes in classification steps, since different units would affect the distance in the feature space.[18] The normal transformation is defined as

$$\hat{\nu}_i = \frac{\nu_i - \mu_i}{\sigma_i},$$

where $\hat{\nu}_i$ is the ith transformed feature, ν_i is the ith original feature, μ_i is the average value of the ith feature, and σ_i is the respective standard deviation. With the normal transformation, all features have mean equal to 0 and standard deviation equal to 1 with respect to the training set.

3. Supervised Classification for Vessel Segmentation

The final segmentation was obtained by classifying the original input image pixels into two classes, namely, vessel pixels and nonvessel pixels, according to the supervised classification approach.[18] A Bayesian classifier was adopted in which class likelihoods were described using Gaussian mixture models, providing a fast classification while still allowing complex decision surfaces. The class priors were estimated by the fraction of each class's pixels

present in a training set composed of labeled samples, while the distribution parameters for each class's Gaussian mixture model were estimated from the training set through the application of the expectation-maximization algorithm.[32]

The training set was obtained from fundus images manually segmented by an ophthalmologist, providing labeled pixels as training samples. The training samples' features were then normalized as described above and used to train the Bayesian classifier. The segmentation of new images was then performed by applying the classifier, without the need of tuning any additional parameters. The segmentation process can be implemented efficiently using the fast Fourier transform and the Fourier-domain definition of the CWT for pixel feature generation,[17] which takes time $\Theta(N \log_2 N)$, where N is the total number of image pixels. The segmentation is obtained applying the Bayesian Gaussian mixture model classifier to all pixels, taking an additional $\Theta(N)$.

Some misclassified pixels appeared as undesirable noise in the output, and as only boundaries were classified for some vessels, it was necessary to perform postprocessing. The postprocessing operations applied were "area open" to eliminate small noisy components, "dilation" and "area close" to fill the vessels, followed by "skeletonization" to extract the vessel branching pattern. The multiscale skeletonization algorithm based on exact dilations has been applied in this last step.[18] Morphological features were then extracted from the obtained vessel skeletons to distinguish such vessel patterns, as described in the next section.

B. Determination of Morphological Features

Automated classification into retinas with or without PDR requires high accuracy to be able to support screening programs currently carried out by ophthalmologists. Seven morphological features associated with the skeletonized vessel pattern were determined: area, perimeter, circularity, curvature, orientation entropy, second moment of the CWT, and correlation dimension, with physical interpretations described as below. With the exception of the area, perimeter, and circularity, all are based on data obtained from the application of the derivatives-of-Gaussian wavelets to the automated segmented vessel skeletons.

1. Area

The area A estimation of the binary skeletons is obtained by simply counting the number of object pixels, taking linear time, $\Theta(N)$ in asymptotic notation, where N is the number of pixels in the image. It provides an approximation of the shape space occupation.

2. Perimeter

The perimeter P is obtained by counting the number of pixels of the vessel skeleton contour, also in linear time $\Theta(N)$.

3. Circularity

The circularity C is just the ratio between the shape square perimeter P and its area A, i.e., P^2/A. It shows how similar the shape is to a circumference and is rotation invariant, being often adopted as a shape complexity measure.[18] This calculation takes time $\Theta(1)$.

4. Wavelet Transform for Morphological Analysis

Different differential morphological features were obtained, inspired by the shape analysis approach used for characterization of retinal ganglion cells.[29] In this paper, we utilized the first derivative of the Gaussian function in order to compose a wavelet gradient. Therefore, we define two analyzing wavelets $\psi_1(x,y)$ and $\psi_2(x,y)$ as partial derivatives of the Gaussian, i.e.,

$$\psi_1(x,y) = \frac{\partial g(x,y)}{\partial x}, \quad \psi_2(x,y) \frac{\partial g(x,y)}{\partial y},$$

where $g(x,y)$ denotes the two-dimensional (2D) Gaussian.[20] By using $\psi_1(x,y)$ and $\psi_2(x,y)$ as wavelets, we can calculate the gradient wavelet as

$$\mathbf{T}_{\psi}[f](\mathbf{b},a) = \begin{pmatrix} T_{\psi_1}[f](\mathbf{b},a) \\ T_{\psi_2}[f](\mathbf{b},a) \end{pmatrix},$$

where ψ, f, $\mathbf{b}$, and a denote, respectively, the analyzing wavelet, the analyzed image, the displacement vector, and the scale factor. The wavelet transform $\mathbf{T}_{\psi}[f](\mathbf{b},a)$ for each pair $(\mathbf{b},a)$ is actually a vector whose components are the respective coefficients of the wavelet transform using $\psi_1(x,y)$ and $\psi_2(x,y)$ as the analyzing wavelets. Since the wavelet transform has been implemented so as to be calculated in the Fourier domain, the calculation of these numerical derivatives take time $\Theta(N \log_2 N)$. The morphological features described below are calculated based on the derivatives-of-Gaussian wavelet.

5. Curvature

The skeleton outline curvature represents how the direction of a unit tangent vector varies along the shape contour. It is described by

$$k = \nabla \cdot \frac{\nabla f}{\|\nabla f\|} = \frac{f_{xx} f_y^2 - 2 f_x f_y f_{xy} + f_{yy} f_x^2}{(f_x^2 + f_y^2)^{3/2}}, \tag{1}$$

where f_x, f_y, f_{xx}, f_{yy}, and f_{xy} denote the first partial derivatives of f with respect to x and y, the second partial derivatives of f with respect to x and y, and the partial derivative with respect to x and y, respectively.[33] These partial derivatives are estimated using the 2D wavelet transform in the same spirit described above for the gradients. Thus, given these partial derivatives, the curvature calculations take additional time $\Theta(N)$.

6. Orientation Entropy

The orientation entropy E indicates the orientation disorder degree encountered in a shape and is obtained from the angular distribution of the vector field defined by the wavelet gradient, as follows:

$$E = -\sum_{i \in K} p_i \ln(p_i), \tag{2}$$

where p_i is the occurrence frequency of some vector oriented toward the θ_i direction and K is the set of bins in the histogram. This calculation takes time proportional to

the number of bins in the histogram, that is, $\Theta(|K|)$.

7. Continuous Wavelet Transform Second Moment

The second moment of the CWT modulus is a statistical dispersion measure to indicate biases in the gradient vector field. If q is the CWT modulus histogram, with each bin q_i centered at i, then its CWT second moment is

$$m_2 = \sum_{i \in K} i^2 q_i. \tag{3}$$

Similarly, this feature is calculated in time $\Theta(|K|)$.

8. Correlation Dimension

According to chaos theory, the correlation dimension (CD) measures the dimension of the space occupied by a set of random points, or in other words, it gives the probability of finding two points closer than a certain distance.[28,34] This probability $C(\varepsilon)$ varies along with the considered distance ε, which ranges between one pixel and the measure of the image diagonal. Usually, one might consider the mean, the median, or the global $C(\varepsilon)$ value. Mathematically, CD is obtained by the correlation integral:

$$C(\varepsilon) = \lim_{N \to \infty} \frac{2}{N^2} \sum_{i=1, j>i}^{N} \theta(\varepsilon - |X_i - X_j|), \tag{4}$$

where the Heaviside function is defined as

$$\theta(\varepsilon - |X_i - X_j|) = \begin{cases} 1 & \text{if } (\varepsilon - |X_i - X_j| \geq 0) \\ 0 & \text{if } (\varepsilon - |X_i - X_j| < 0), \end{cases} \tag{5}$$

and the CD itself is taken as the slope of the logarithm of the correlation integral:

$$C(\varepsilon) \propto \varepsilon^{CD}. \tag{6}$$

The CD curve itself is composed of several short straight segments, among which the first and the last should be disregarded, since in those regions the scales ε do not bring significant fractality information from the shape.[35]

To determine the upper and lower bounds that are the singularities, we calculated the third derivative. The third derivative locates critical points found by the second derivative by searching for zero crossing points.[36] Hence, to find these region extremities, that is, singularities, we calculated the third derivative from $C(\varepsilon)$, determining its zero crossing points, where those abrupt changes in slope take place. The third derivative provides a vector of extremities for each segment of the curve. Thus by using the third-derivative information, we ignore the first and the last segments, sort the remaining ones, and take the median value, resulting in the median CD value. The global CD value is obtained by disregarding the first slope segment and the last one and then by considering the straight line between the points related to the second zero crossing and the penultimate point in order to evaluate the global slope. The correlation integral [Eq. (4)] takes time $\Theta(N^2)$, being the most time-consuming feature calculation, while its derivative calculations take an additional $\Theta(N \log_2 N)$.

C. Statistical Analysis

Results for the features associated with automated and manual segmentations were compared using a two-sample t-test with unequal variance to test the hypothesis that the means were not significantly different. Linear discriminant analysis (LDA) was performed on the matrix representing the data for each of the images (no retinopathy/background retinopathy versus PDR). Matrices were normalized so that each feature has zero mean and unit standard deviation followed by linear regression

A forward–backward feature-selection process using LDA as the classifier was also applied to select the best features. This process can be shown to be a monotonically increasing function of the signal-to-noise ratio and, using the area under the curve (AUC), indicates the effectiveness of the feature in discriminating between the two groups.

3. RESULTS

The classifier output obtained from the original image is a binary image with labeled pixels as vessel or nonvessel. This binary image is postprocessed and skeletonized, producing the results as illustrated in Fig. 1.

Figure 2 compares the outcome of the pattern analysis for orientation entropy and correlation integral for an image with and one without proliferative retinopathy.

Table 1 lists statistics of the seven features calculated between the manual and the automated segmented images. Manual segmented images resulted in larger feature parameters, except for circularity. A student t-test showed that the differences between the means of all features are statistically significant ($p < 0.001$), except for the entropy ($p = 0.38$). The differences arise because more vessels are identified by the observer than by the automated procedure.

Since we are interested primarily in automated detection of PDR, we proceed to further analyze the automated data only. These data were normalized so that each feature has zero mean and standard deviation of one. The ability to use each feature individually to discriminate between non-PDR and PDR is summarized in Table 2. Only the curvature feature achieves statistical significance ($p = 0.042$) for a two-sampled t-test for the difference in means between the non-PDR and the PDR classes. However we are more interested in classification ability, and the AUC of the parametric binormal receiver operating characteristic (ROC) was also calculated.[37] The traditional features (area, perimeter, and circularity) and the global CD are essentially random and thus have no classification ability (AUC = 0.49 in all cases). The wavelet-based features (second moment, entropy, curvature, and median CD) have some useful classification ability, with AUCs of about 0.7. This indicates that these latter features are indeed more sensitive to the blood vessel branching patterns throughout the retina.

The above analysis considered features in isolation. A combination of features with an appropriate classifier may provide better predictive ability. We first tried forward–backward selection of features using the linear discriminant and naïve-Bayes classifiers.[32] The AUC calculated from the resultant classifier was used as the cri-

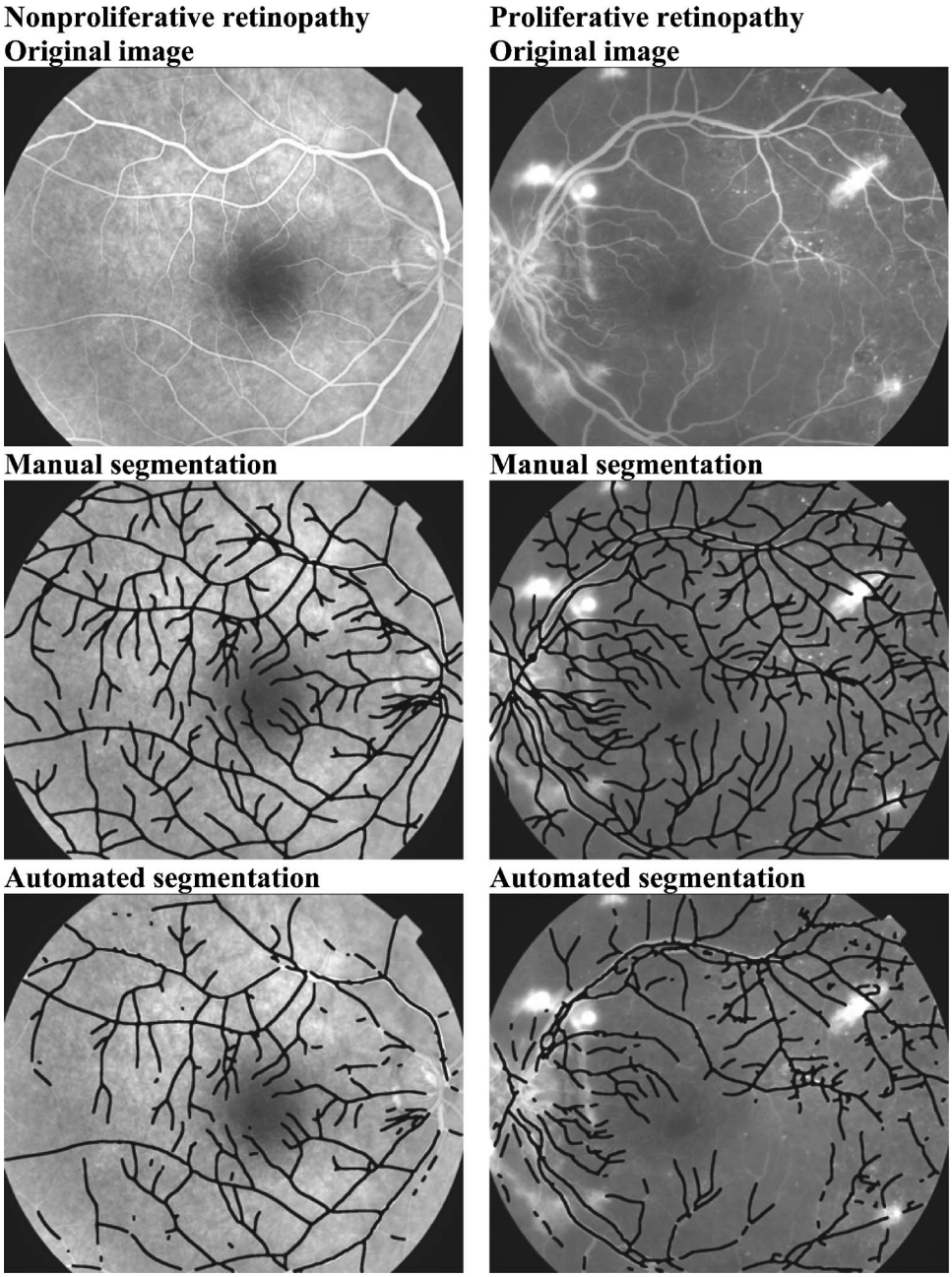

Fig. 1. Illustration of outcome for automated and manual segmentation compared with the original gray-scale image. Overlaid skeletonized vessel pattern, in black, has been dilated for easier viewing.

terion for selection or removal of features. We report AUCs with 95% confidence intervals (CIs) as calculated by the ROCKIT program.[37] The best features identified using forward–backward selection on the LDA classifier were median CD and wavelet second moment with an AUC of 0.77 (0.56–0.91). Starting with all features and removing any that improved classification led to a set of six features (area, perimeter, entropy, curvature, median CD, and global CD), with the LDA classifier achieving an AUC of 0.90 (0.73–0.97). As we are interested in the improvement provided by the wavelet-based features, we also ran LDA on the feature set comprising area, perimeter, and circularity only, which achieved an AUC of 0.61 (0.37–0.82). Note that LDA-based classification using traditional features (area, perimeter, and circularity) fails statistical significance for better than random classification at 95% confidence, whereas the wavelet-based feature achieves a statistically significant power to discriminate between PDR and non-PDR.

The naïve-Bayes classifier shows similar results. Using just area, perimeter, and circularity, a naïve-Bayes classifier has an AUC of 0.58 (0.37–0.78) and fails statistical significance for better than random discriminatory power. Using the best four features (area, second moment, entropy, and global CD) identified by forward–backward selection gives an AUC of 0.87 (0.67–0.96), which has statistically significant and useful discriminatory power. For the naïve-Bayes classifier, as with LDA, it is necessary to include some of the wavelet-based features to discriminate between PDR and non-PDR.

We show in Fig. 3 the full ROC curve (fitted to the data with the parametric binormal model due to Metz) for the LDA classifier operating on the best six features identified above and the ROC curve fitted to the LDA classifier operating on the traditional three features.

Using the best six features and the LDA classifier at the operating point marked with an asterisk on the ROC curve (Fig. 3), three images were incorrectly classified. Of these, one was opaque and of bad quality, while the second had a venous loop present. The third was of good quality with neovascularization present both near the disk and in the periphery. Thus the classifier achieved 15 true positives out of 16 images (sensitivity of 94%) and 2 false positives out of 11 negatives (false-positive rate of 18%), giving a specificity of 82% using automatically segmented images.

4. DISCUSSION

The importance of our work lies in combining automated segmentation procedures with automated recognition of proliferative retinopathy using features determined from the wavelet-derived results such as second wavelet moment, entropy, and median CD. In addition we have aimed to use a clinically relevant sample that included images where the quality was not optimal and those with panretinal laser surgery scars, diverse progression of retinopathy, and proliferation showing either as areas of ischaemia or as new blood vessels near the optic disk or in the periphery. The results obtained were produced using the same configuration parameters for all images; preprocessing and optic disc removal to improve the vessel segmentation were also not required owing to the nature of

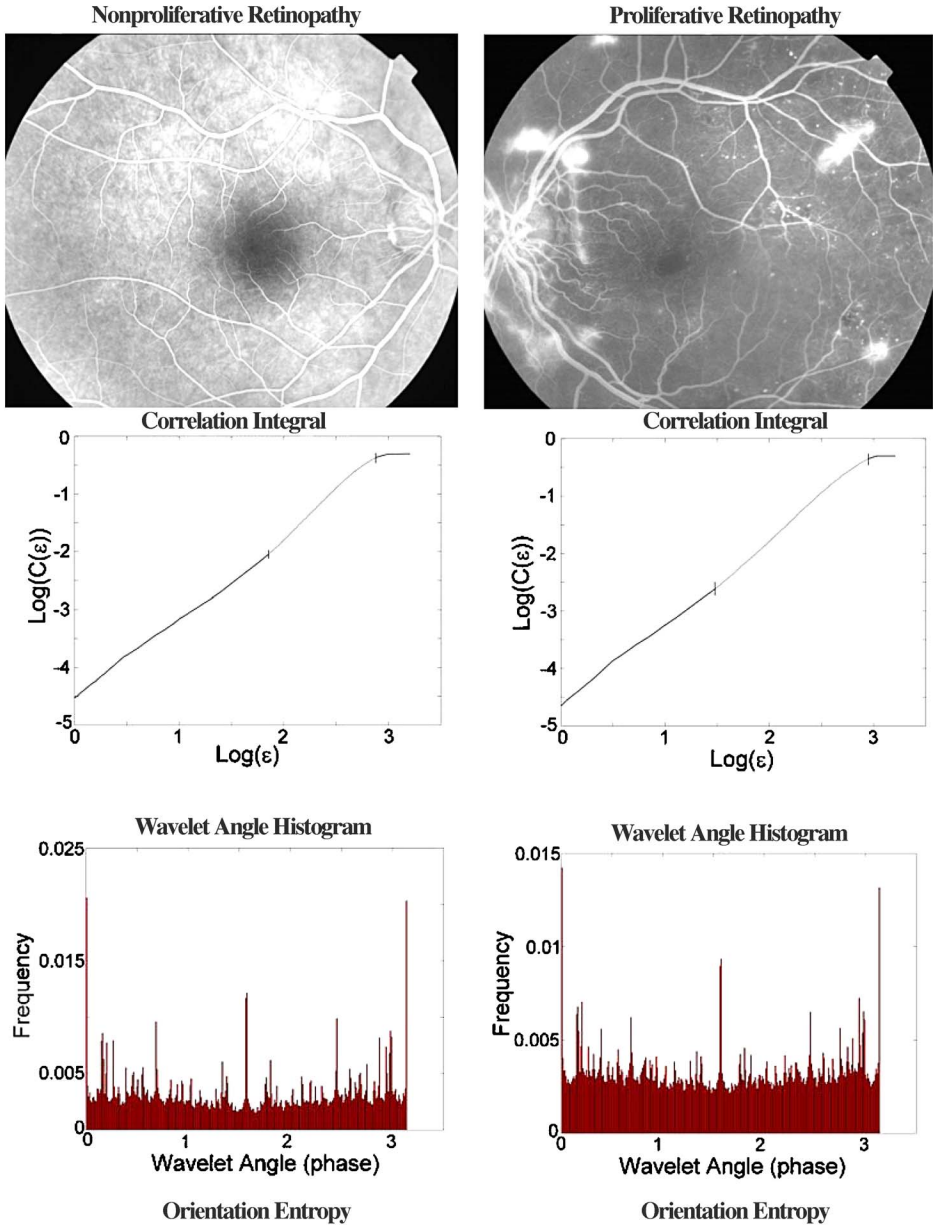

Fig. 2. (Color online) Correlation integral and wavelet histogram for the orientation entropy comparing an image with neovascularization to one with no neovascularization. Vertical lines on the log–log correlation integral indicate upper and lower bounds (see text).

Table 1. Feature Comparison for Manual and Automated Segmented Images

Feature	Manual Segmentation (Mean±SD)[a]	Automated Segmentation (Mean±SD)	*t*-Statistic	*p*-Value
Area	102,000±23,000	24,600±5200	−17.0	<0.0001
Perimeter	31,200±5200	24,400±8400	−6.74	<0.0001
Circularity	13,500±3000	24,300±5100	9.38	<0.0001
Second moment	4362±25	1080±24	−493	<0.0001
Entropy	5.63±0.01	5.62±0.02	−0.9	0.38[b]
Curvature	178.0±3.9	133.6±4.3	−39.9	<0.0001
Median CD[c]	1.67±0.1	1.42±0.1	−11.8	<0.0001
Global CD	1.58±0.04	1.49±0.04	−8.2	<0.0001

[a]Mean ± standard deviation.

[b]Nonsignificant.

[c]Correlation dimension.

Table 2. Comparison between Nonproliferative and Proliferative Diabetic Retinopathy for the Eight Features Analyzed

Feature	Non-PDR	PDR	*t*-Statistic	*p*-Value	AUC[a]
Area	0.038±0.82	−0.026±1.1	0.169	0.87	0.49
Perimeter	0.040±0.82	−0.027±1.1	0.178	0.86	0.49
Circularity	0.041±0.82	−0.029±1.1	0.186	0.85	0.49
Second moment	−0.35±0.63	0.24±1.1	−1.74	0.095	0.72
Entropy	−0.41±1.3	0.28±0.65	−1.64	0.12	0.70
Curvature	−0.46±0.85	0.31±1.0	−2.15	0.042	0.76
Median CD[b]	−0.44±1.1	0.30±0.87	−1.93	0.068	0.70
Global CD	−0.065±0.82	0.45±1.1	−0.292	0.77	0.49

[a]Area under curve.

[b]Correlation dimension.

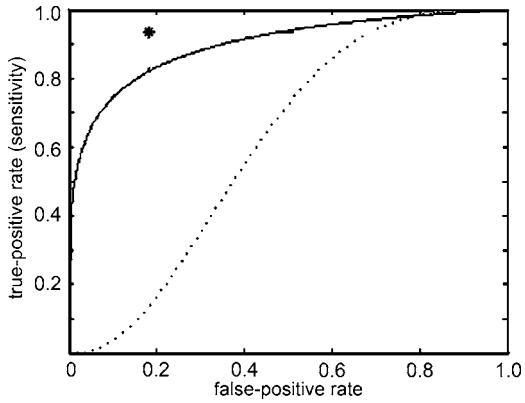

Fig. 3. ROC curve for automated segmented images using the set of six best features. ∗ is operating point; solid curve, six best features; dashed curve, traditional features (area, perimeter, circularity).

the wavelet transform. This is a major step forward in automated segmentation and analysis, as it decreases the computation time and operator involvement.[10] Nevertheless differences between manual and automated segmentation can be noted (Fig. 1). Quality of an image associated either with methodology or with pathology influences not only automated methods but also manual segmentation, as can be seen in the STARE database (http://www.parl.clemson.edu/stare/). These errors are, however, randomly distributed across the nonproliferative and proliferative retinopathy images and should not have influenced the outcome of our classification.

Previous work comparing the CWT with other segmentation methods using the STARE and DRIVE database images as the gold standard showed that supervised learning and adaptive thresholding obtained a greater than 75% sensitivity for vessel segmentation.[15] A comparison of six segmentation methods, including our CWT, indicated a similar outcome, with the sensitivity and specificity being greater then 80%.[16]

Ophthalmologists have an 80% to 95% success rate in identifying proliferative retinopathy. This success rate decreases with eye media opacification and for identifying earlier stages of proliferation. However nonspecialists perform no better than chance (50%).[38] Traditional features such as area or perimeter are not sensitive enough to discriminate between the nonproliferative retinopathy and the retinal fundi displaying neovascularization. This is because area and perimeter pick up only the total amount of vasculature, whereas PDR involves a reconfiguration of the vasculature. It is necessary therefore to use features that are sensitive to the branching and space-filling nature of the vessel pattern, such as the wavelet-based features that we employed.

Our feature analysis suggests that utilizing the six best features, which include median correlation dimension, curvature, and entropy, provides the most accurate clas-

sification, with 94% sensitivity and 82% specificity. The three images classified incorrectly included one with opacity, while another had advanced nonproliferative retinopathy, and the third had a venous loop and Hollenhorst plaques in addition to the presence to diabetic retinopathy. As such, including additional image analysis tools such as a microaneurysm detector may improve these findings. The use of digital nonmydriatic color images for routine community screening has been shown to be effective but will lead to a further challenge for detecting early-stage proliferative retinopathy using automated methods. In addition, classifiers other than the LDA or naïve-Bayes reported here may also improve the classification results, and this is currently being investigated on a larger set of images.

One of the advantages of our morphological feature set is that it identified images that contain neovascularization within the retina but not in the view of the posterior pole, suggesting that peripheral changes associated with neovascularization lead to a remodeling throughout the retina.

ACKNOWLEDGMENTS

Herbert Jelinek was in receipt of a Charles Sturt University grant (A514 713 9661). Roberto M. Cesar, Jr., and João V. B. Soares are grateful to State of São Paulo Research Foundation (FAPESP) (2005/00587-5 and 2006/56128-1) and to National Council of Technological and Scientific Development (CNPq) (300722/98-2, 474596/2004-4, 131403/2004-4, and 491323/2005-0). We thank Cherryl Kolbe and Bev deJong for technical assistance. Chris McQuellin was responsible for the retinal photography.

Corresponding author Herbert Jelinek can be reached by e-mail at hjelinek@csu.edu.au.

REFERENCES

1. H. R. Taylor and J. E. Keeffe, "World blindness: a 21st century perspective," Br. J. Ophthamol. **85**, 261–266 (2001).
2. K. Viswanath and M. McGavin, "Diabetic retinopathy: clinical findings and management," Community Eye Health **16**, 21–24 (2003).
3. K. S. Coyne, M. K. Margolis, T. Kennedy-Martin, T. M. Baker, R. Klein, M. D. Paul, and D. A. Revicki, "The impact of diabetic retinopathy: perspectives from patient focus groups," Fam. Pract. **21**, 447–453 (2004).
4. J. Kanski, *Clinical Ophthalmology: A Systematic Approach* (Butterworth-Heinemann, 1989), pp. 465–479.
5. U. Freudentsin and J. Verne, "A national screening programme for diabetic retinopathy," BMJ **323**, 4–5 (2001).
6. S. J. Lee, C. Sicari, C. A. Harper, H. R. Taylor, and J. E. Keeffe, "Program for the early detection of diabetic retinopathy: a two-year follow-up," Clin. Exp. Optom. **29**, 12–25 (2001).
7. T. Walter, J. C. Klein, P. Massin, and F. Zana, "Automated segmentation and registration of retinal fluorescein angiographies," presented at the First International Workshop on Computer Assisted Fundus Image Analysis (CAFIA), Herlev Hospital, Copenhagen, Denmark, May 29–30, 2000.
8. X. W. Gao, A. Bharath, A. Stanton, A. Hughes, N. Chapman, and S. Thorn, "Quantification and characterisation of arteries in retinal images," Comput. Methods Programs Biomed. **63**, 133–146 (2000).
9. A. Hoover, V. Kouznetsova, and M. Goldbaum, "Locating blood vessels in retinal images by piecewise threshold probing of a matched filter response," IEEE Trans. Med. Imaging **19**, 203–210 (2000).
10. F. Zana and J.-C. Klein, "Segmentation of vessel-like patterns using mathematical morphology and curvature evaluation," IEEE Trans. Image Process. **10**, 1010–1019 (2000).
11. C. Kirbas and F. Quek, "A review of vessel extraction techniques and algorithms," ACM Comput. Surv. **32**, 81–121 (2004).
12. X. Jiang and D. Mojon, "Adaptive local thresholding by verification-based multithreshold probing with application to vessel detection in retinal images," IEEE Trans. Pattern Anal. Mach. Intell. **25**, 131–137 (2003).
13. J. J. Staal, M. D. Abràmoff, M. Niemeijer, M. A. Viergever, and B. van Ginneken, "Ridge based vessel segmentation in color images of the retina," IEEE Trans. Med. Imaging **23**, 501–509 (2004).
14. D. Nain, A. Yezzi, and G. Turk, "Vessel segmentation using a shape driven flow," presented at the Medical Image Computing and Computer-Assisted Intervention (MICCAI), Saint-Malo, France, September 26–29, 2004.
15. D. Cornforth, H. F. Jelinek, J. J. G. Leandro, J. V. B. Soares, R. M. Cesar, Jr., M. J. Cree, P. Mitchell, and T. Bossomaier, "Evolution of retinal blood vessel segmentation using wavelet transform in assessment of diabetic retinopathy," Complexity International **11**, 50–60 (2005), http://www.complexity.org.au/ci/vol11/.
16. M. J. Cree, J. J. G. Leandro, J. V. B. Soares, R. M. Cesar, Jr., H. F. Jelinek, and D. Cornforth, "Comparison of various methods to delineate blood vessels in retinal images," in *Proceedings of the 16th Australian Institute of Physics Congress* (AIP, 2005) pp. 1–4.
17. J. V. B. Soares, J. J. G. Leandro, R. M. Cesar, Jr., H. F. Jelinek, and M. J. Cree, "Retinal vessel segmentation using the 2-D Gabor wavelet and supervised classification," IEEE Trans. Med. Imaging **25**, 1214–1222 (2006).
18. L. F. Costa and R. M. Cesar, Jr., *Shape Analysis and Classification: Theory and Practice* (CRC, 2001).
19. J. P. Antoine, D. Barache, R. M. Cesar, Jr., and L. F. Costa, "Shape characterization with the wavelet transform," Signal Process. **62**, 265–290 (1997).
20. A. Arnéodo, N. Decoster, and S. G. Roux, "A wavelet-based method for multifractal image analysis. I. Methodology and test applications on isotropic and anisotropic random rough surfaces," Eur. Phys. J. B **15**, 567–600 (2000).
21. A. Grossmann, "Wavelet transforms and edge detection," in *Stochastic Processes in Physics and Engineering*, S. Albeverio, P. Blanchard, M. Hazewinkel, and L. Streit, eds. (Reidel, 1988), pp. 149–157.
22. M. J. Cree, J. A. Olson, K. McHardy, P. Sharp, and J. Forrester, "A fully automated comparative microaneurysm digital detection system," Eye **11**, 622–628 (1997).
23. J. Hipwell, F. Strachan, J. Olson, K. McHardy, P. Sharp, and J. Forrester, "Automated detection of microaneurysms in digital red-free photographs: a diabetic retinopathy screening tool," Diabetic Med. **17**, 588–594 (2000).
24. C. Sinthanayothin, J. F. Boyce, H. Cook, and T. Williamson, "Automated localisation of the optic disc, fovea and retinal blood vessels from digital colour fundus images" Br. J. Ophthamol. **83**, 902–912 (1999).
25. A. Osareh, M. Mirmehdi, B. Thomas, and R. Markham, "Automated identification of diabetic retinal exudates in digital colour images," Br. J. Ophthamol. **87**, 1220–1223 (2003).
26. M. E. Martinez-Perez, A. D. Hughes, A. V. Stanton, S. A. Thom, N. Chapman, A. A. Bharath, and K. H. Parker, "Retinal vascular tree morphology: a semi-automatic quantification," IEEE Trans. Biomed. Eng. **49**, 912–917 (2002).
27. R. M. Cesar, Jr., and H. F. Jelinek, "Segmentation of retinal fundus vasculature in nonmydriatic camera images using wavelets," in *Angiography and Plaque Imaging*, J. S. Suri and S. Laxminarayan, eds. (CRC, 2003), pp. 193–224.
28. B. R. Masters, "Fractal analysis of the vascular tree in the

human retina," Annu. Rev. Biomed. Eng. **6**, 427–452 (2004).
29. H. F. Jelinek, R. M. Cesar, Jr., and J. J. G. Leandro, "Exploring wavelet transforms for morphological differentiation between functionally different cat retinal ganglion cells," Brain and Mind **4**, 67–90 (2003).
30. J. P. Antoine, P. Carette, R. Murenzi, and B. Piette, "Image analysis with two-dimensional wavelet transform," Signal Process. **3l**, 241–272 (1993).
31. J. J. G. Leandro, J. V. B. Soares, R. M. Cesar, Jr., and H. F. Jelinek, "Blood vessel segmentation of non-mydriatic images using wavelets and statistical classifiers," in *Proceedings of the Brazilian Conference on Computer Graphics, Image Processing and Vision* (Sibgrapi, 2003), pp. 262–269.
32. R. O. Duda, P. E. Hart, and D. G. Stork, *Pattern Classification*, 2nd ed. (Wiley Interscience, 2001).
33. L. F. Estrozi, L. G. Rios, A. G. Campos, R. M. Cesar, Jr., and L. d. F. Costa, "1D and 2D Fourier-based approaches to numeric curvature estimation and their comparative performance assessment," Digit. Signal Process. **13**, 172–197 (2003).
34. P. Asvestas, G. K. Matsopoulos, and K. S. Nikita, "Estimating of fractal dimension of images using fixed mass approach," Pattern Recogn. Lett. **20**, 347–354 (1999).
35. J. P. Rigaut, "An empirical formulation relating boundary lengths to resolution in specimens showing 'non-ideally fractal' dimensions," J. Microsc. **133**, 41–54 (1984).
36. R. C. Gonzalez, R. E. Woods, and S. L. Eddins, *Digital Image Processing Using Matlab* (Pearson Prentice Hall, 2004).
37. C. E. Metz, "ROC methodology in radiologic imaging," Invest. Radiol. **21**, 720–733 (1986).
38. E. Sussman, W. Tsiaras, and K. Soper, "Diagnosis of diabetic eye disease," J. Am. Med. Assoc. **247**, 3231–3234 (1982).